J. Fluid Mech. (2005), *vol.* 544, *pp.* 69–97.
doi:10.1017/S0022112005006531 Printed in the United Kingdom

Baroclinic instability of two-layer vortices in laboratory experiments

By E. THIVOLLE-CAZAT, J. SOMMERIA AND M. GALMICHE

LEGI/Coriolis, UMR 5519, 21 Avenue des Martyrs, 38000 Grenoble, France

(Received 28 August 2003 and in revised form 1 June 2005)

The dynamics of a baroclinic vortex in a two-layer rotating stratified fluid is investigated. The vortex is produced by the classical geostrophic adjustment process, starting from an initial step in the layer interface. The experiments are performed on the 13 m diameter Coriolis turntable, allowing investigation of inertial regimes, in which viscous friction effects are negligible. The velocity fields are measured in both layers by employing particle image velocimetry, thus providing a quantitative measure of the flow evolution.

The baroclinic instability occurs much later in time than the initial inertial oscillations. The growth occurs in a hydrostatic regime, with velocity being independent of height in each layer. This process is described well by linear stability theory for a quasi-geostrophic disk vortex, or by the classical model of Phillips (1954) empirically adapted to the circular geometry. This stability prediction from the quasi-geostrophic model remains relevant even for a large initial interfacial step. For strong cyclones, the instability grows roughly twice as fast as these predictions.

In the nonlinear stage of the instability, the initial vortex splits and reorganizes into vortex pairs propagating outward. These dipoles involve the interactions of positive and negative vortices, with components in the upper and in the lower layer. In the case of a large initial interface step, a clear asymmetry between anticyclones and cyclones is observed: the latter are more intense and compact, with a more barotropic structure.

Our results are compared with numerical simulations, using a two-layer isopycnal model. Data assimilation is used to initiate the model with the same perturbations as in the laboratory experiments, thus providing a quantitative test of the dynamics. Furthermore, data assimilation is used to extrapolate the measurements, yielding the interface position and potential vorticity fields.

1. Introduction

Vortices are ubiquitous features of the atmosphere and oceans. In the Earth's atmosphere, synoptic vortices control the weather system at mid-latitudes (Pierrehumbert & Swanson 1995). In the ocean, meso-scale vortices are formed by instabilities of the Gulf Stream. These vortices trap fluid in their core, and are responsible, because of their long lifetime, for long distance transport of heat and salinity. Such vortices are able to split into several secondary vortices. These processes have been well documented for the Gulf Stream system. Richardson, Maillard & Stanford (1979) described the splitting of a vortex "Allen" into two cyclones. Kennelly, Evans & Joyce (1985) observed the formation of ringlets of typically six cyclones around an anticyclonic eddy detached from the Gulf Stream.

These vortices are confined to the warmer upper oceanic layer (typically 500 m deep), and float on the underlying more dense water, with slower motion. Considering this stratification as a two-layer system, the splitting process is well understood as a consequence of baroclinic instability. A prototype of this instability is provided by the quasi-geostrophic model of Phillips (1954), assuming a uniform velocity, different in each layer. An extension of this model to a circular vortex with a uniform-potential-vorticity disk core, with opposite sign in each layer, is discussed by Sokolovskiy & Verron (2000). Numerical simulations indicate vortex splitting into several secondary vortices, followed by a reorganization of each secondary vortex into a vortex dipole called a 'heton' (Hogg & Stommel 1985). This steadily translating structure couples a positive vortex in one layer to a negative vortex in the other, and the velocity induced by each vortex drives the translating motion of the other one. The theory of baroclinic instability predicts a maximum growth rate for wavelengths of the order of the Rossby radius of deformation L_R. Accordingly, the observed size of the secondary vortices is of order L_R and their number scales like R/L_R, where R is the initial vortex radius.

While the quasi-geostrophic model is strictly valid for small interface displacements, theory and numerical simulations for a general two-layer system indicate that the stability properties remain comparable to the quasi-geostrophic results. The change is only quantitative, with a faster instability growth for cyclones than for anticyclones, while the two cases are symmetric in the quasi-geostrophic limit (Stegner & Dritschel 2000; Baey & Carton 2002). The comparability with the quasi-geostrophic results persists even in the case of an outcroping interface, for which the layer thickness vanishes at a front (Boss, Paldor & Thompson 1996).

The possibility of more complex effects is, however, predicted for vortex structures involving both baroclinic and barotropic components (see Carton 2001 for a review). For instance some non-normal modes can grow to a large amplitude by transient amplification, and nonlinear instability by resonance of neutral waves can occur. Nonlinear stabilization into tripolar vortices has also been observed.

The relevance of these theoretical and numerical approaches to real vortices is thus of interest. The vortex structure is not arbitrary but results from some initial relaxation process, influenced by turbulent mixing. Laboratory experiments allow reproduction of such flow phenomena under well-controlled conditions, in dynamical similitude with natural systems.

Turntable experiments on baroclinic vortex instabilities have been performed by Saunders (1973), and Griffiths & Linden (1981*a*). In the 'constant volume' experiments, Griffiths & Linden (1981*a*) produced a vortex by releasing dyed buoyant fluid on the surface of a denser fluid. Qualitative agreement with the Phillips model of baroclinic instability was observed, although the experimental vortices were not quasi-geostrophic: they were produced on an upper layer of limited extent, bounded laterally by fronts. Numerical simulations of the experiments have been performed by Verzicco, Lalli & Campana (1997), using a fully three-dimensional model. They found good agreement with the laboratory results, and were able to obtain more quantitative comparisons with theory, and to analyse the energy exchanges.

Similar experiments, using a larger vortex, close to the size of the rotating tank, have been performed to study the instability of fronts near an outer boundary by Griffiths & Linden (1981*b*), Chia, Griffiths & Linden (1982), Holford & Dalziel (1996) and Bouruet-Aubertot & Linden (2002).

Such previous experiments were mostly limited to visualization and qualitative results, and the role of viscosity and surface tension is unclear at such scales. Baroclinic

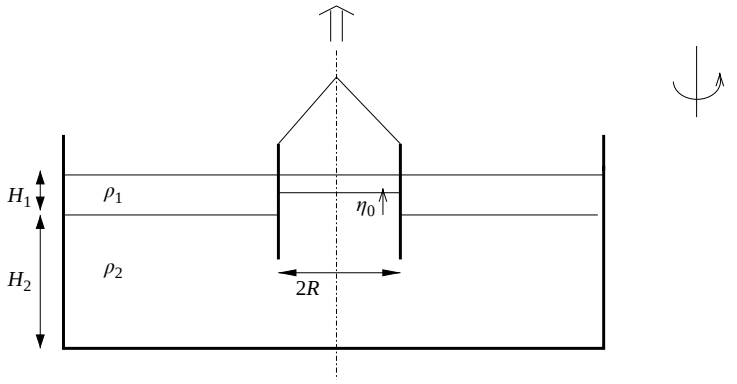

FIGURE 1. Sketch of the experimental system. A layer interface with a step η_0 is produced when the cylinder is lifted.

instabilities have also been produced in annular rotating tanks with lateral heating and cooling, as discussed for instance by Hide & Mason (1975) and Read *et al.* (1992). Viscosity effects, as well as thermal diffusion, are also important in such experiments. There is a need for quantitative experiments on baroclinic instability in the inertial regimes typical of the atmosphere or the oceans, which involve mixing by small-scale turbulence rather than by viscous diffusion.

We present here experiments on baroclinic instability, repeating the procedure of Griffiths & Linden (1981*a*). Our vortex is ten times larger in diameter and thickness however, providing a closer physical realization of an inviscid two-layer system. This is made possible by using the 13 m diameter 'Coriolis' turntable. The time-evolving velocity field is accurately monitored, using particle imaging velocimetry (PIV). Finally, a data assimilation system is used to provide optimized initial conditions for a two-layer numerical model, including the small perturbations at the origin of the instability. This allows us to extrapolate the measured fields, providing in particular the interface displacement and potential vorticity fields. By switching off the data assimilation at different times, we are able to assess how the model evolution departs from the experiments at the different stages of the dynamics.

The plan for the paper is to discuss the experimental and numerical procedure in § 2. The axisymmetric vortex structure resulting of the geostrophic adjustment is analysed in § 3, and compared with predictions for geostrophic adjustment. The growth of the baroclinic instability and its nonlinear development are discussed in § 4 and § 5 respectively. We conclude in § 6.

2. Experimental procedure and data analysis

2.1. *Experimental device*

The experimental system is sketched in figure 1. The rotating tank is first filled with a lower layer of salt water with density ρ_2. The second layer, of density ρ_1, is made by slowly pouring lighter water through floating porous plates. To prepare the vortex generation, a vertical bottomless cylinder, with diameter $2R = 1$ m, is introduced and the layer interface is displaced by an amount η_0 inside, by pumping the upper layer fluid in or out, leading to negative or positive η_0 respectively. After the pumping, the system is left until it reaches an initial state of rest (after about one hour). In this state, the upper layer has a thickness $H_1 = 12.5$ cm outside and $H_1 - \eta_0$ inside, while the lower

layer has thickness H_2 outside the cylinder and $H_2+\eta_0$ inside the cylinder. As limiting cases, experiments are also performed with an upper layer introduced only inside the cylinder ($H_1=0$, $\eta_0=-12.5$ cm), and only outside the cylinder ($H_1=12.5$ cm, $\eta_0=12.5$ cm). In all cases the total water thickness is $H=H_1+H_2=62.5$ cm.

A constant tank rotation period $T=50$ s is used for all of the experiments. The rotation is anticlockwise, so that cyclones are seen to rotate in the positive trigonometric direction. The layer filling and experiment preparation are done after the rotation is already established, to avoid spin-up effects. The centrifugal force results in a slightly tilted apparent gravity, leading to a (weakly) parabolic layer interface and free surface at rest. The initial upper-layer thickness H_1 is therefore constant outside the cylinder, while the lower-layer thickness varies by 3.4 cm from the tank centre to periphery. The reference thickness H is defined at the radius of the cylinder centre (2.5 m). Its variation is weak, $\delta H/H=0.7\,\%$, over the vortex scale 1 m.

At the starting time $t=0$, the cylinder is quickly lifted out by a vertical translation system. It crosses the upper layer in less than 1 s, negligible in comparison with the dynamical evolution. The cylinder wall is thin (5 mm thick), with a chamfered edge, so its wake during lifting is limited to a narrow region with negligible influence on the global dynamics. Therefore the initial condition can be considered as the state of rest with a step in the interface. After being lifted, the cylinder is quickly moved aside by a carriage to clear the field of view from above.

The cylinder is at the centre of the zone under study and bounded laterally by vertical walls to minimize wind effects resulting from the tank rotation. These walls are at least 2 m away from the cylinder so that confinement effects are not significant. Furthermore, the walls are covered with plastic trellis to damp inertia–gravity waves.

Various experiments are performed with different values of the relative density difference $\delta\rho/\rho=(\rho_2-\rho_1)/\rho_1$ between the salt-water layers and different values of the interface step η_0, as summarized in table 1 below. Before each experiment, the vertical profile of salinity and temperature is measured inside and outside the cylinder; see figure 2 for an example. This yields the layer thickness and displacement η_0 and confirms that the interface is sharp. The density is controlled principally by the salinity. The temperature of the water is set to room temperature during filling, such that the difference between the upper and lower layer is always less than 1 °C (corresponding to $\delta\rho/\rho<0.25\ 10^{-3}$).

2.2. *Measurement techniques*

The velocity field is measured in a number of horizontal planes using particle image velocimetry (PIV), as described in Fincham & Spedding (1997) and Fincham & Delerce (2000). Seeding particles are introduced in both layers, and illuminated by a laser sheet (using a classical 8 W argon laser). Images are taken from above by a digital CCD camera with spatial resolution 1024×1024 pixels. Each velocity field is obtained from a burst of four images, allowing a choice of an optimum time interval for the image inter-correlations (the particle displacement between two images must be about 5–10 pixels).

The field of view is 2.5 m × 2.5 m, centred on the cylinder axis. In a few experiments, the upper layer is dyed with fluorescein, so the layer interface is made visible by laser-induced fluorescence (LIF). For that application, the line at 488 nm of the argon laser is used, and the sheet is vertical.

The size of the seeding particles must be sufficiently large to be visible to the camera: their diameters range between 200 and 400 μm. Sedimentation is a major

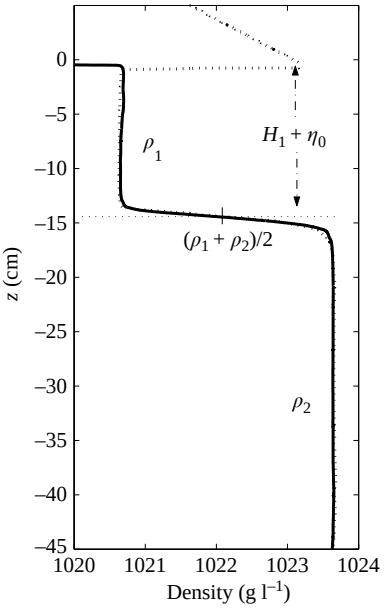

FIGURE 2. Density profile inside the cylinder measured by translating probes (at speed 1 cm s^{-1}) just before an experiment. Density is obtained from measurements of salinity (solid curve) or ultrasound propagation speed (dotted line), taking into account a correction for the temperature variations, which is small (it is measured by a thermistor probe).

problem, and the particle density must be carefully matched with water. Pliolite particles are used, with a density of 1025 g l^{-1}. The density of the lower water layer is adjusted by salt concentration slightly below this value, so that the particles slowly sediment toward the bottom instead of accumulating at the interface. One hour before each experiment, a flat rod is moved along the bottom of the tank in order to lift the particles in the lower layer (according to Stokes' law, the sedimentation speed of a particle 300 μm in diameter and a density difference of 1 g l^{-1} is 7 cm per hour, so most particles remain suspended during the experiment). To seed the upper layer, a suspension of particles is sprayed over the area of study just before the experiment. This produces a significant level of disturbances by small-scale eddies.

The laser sheet (5 mm thick) is generally positioned at the middle of each layer (at $z = 6.25$ cm from the free surface for the upper layer and $z = 37.5$ cm for the lower layer). It is alternately switched between these two positions by a translating mirror. Then a field is obtained at period 11 s at each level (this sampling is at half the period of the observed inertial oscillations to avoid aliasing effects).

The velocity fields at each level are obtained on a regular square grid of 100×100 points, from which vorticity can be calculated by spline smoothing interpolation and differentiation. A similar spline is used to obtain the velocity on a circle around the cylinder. Details on the PIV processing can be obtained at http://www.civproject.org/documentation.htm.

2.3. *Numerical model and data assimilation*

We have performed numerical simulations of the experiments, using the Miami Isopycnic Coordinate Ocean Model (MICOM), which has already been used extensively for oceanic problems (Bleck & Boudra 1986). The physical system is modelled as a multi-layer fluid with the hydrostatic approximation. The variables are

the horizontal velocity components u and v, and the layer thickness h for each layer. We use a simplified version here, with only two layers, and a square domain. The spatial scheme has been improved to preserve the conservation laws at fronts where a layer outcrops at the surface (Y. Morel, private communication). Small-scale velocity fluctuations are smoothed out by a standard biharmonic dissipation term. Note that there is no vertical diffusion: this is a fundamental property of isopycnal models.

When comparing a model with laboratory experiments, the determination of the initial condition is an important issue. This is particularly so in the case of unstable flows, as the whole evolution depends sensitively on the structure of the initial perturbation. We measure the initial velocity field, but not the corresponding interface displacement. An hypothesis of cyclogeostrophic balance could be used for that purpose, following for instance Verron & Valcke (1994). We have used instead a more complex technique of data assimilation, which aims at providing an optimal blend between a numerical prediction and a set of measurements. A motivation of the present work was to test such data asimilation techniques in the well-controlled conditions of laboratory experiments, see Galmiche *et al.* (2003). However we did not compare the results with more simple methods, so we do not claim that this technique is superior for the purpose of model initiation.

Data assimilation techniques were first developed to update weather forecasts which optimally utilize available observational data. We use here the Singular Evolutive Extended Kalman (SEEK) filter, a method adapted for oceanographic purposes on the basis of the Kalman filter (see Pham, Verron & Roubaud 1998 for mathematical details). The measured velocity field in both layers is assimilated into the model simulations at each grid point in the measurement domain ($2.5\,\mathrm{m} \times 2.5\,\mathrm{m}$). The simulations are performed with the same grid mesh, but in a domain twice the size ($5\,\mathrm{m} \times 5\,\mathrm{m}$), to avoid spurious confinement by boundaries. The fields are measured in each layer every 11 s, which is half the observed period of the inertial oscillations. Since we are interested in slow-balanced dynamics, we eliminate the residual inertial oscillations by averaging over two successive fields for data assimilation. This helps to prevent the excitation of spurious inertial waves as they are introduced by the data assimilation.

2.4. *Parameters*

The dynamics of the system is controlled by eight physical parameters (neglecting the interface thickness h): the cylinder radius R, the thickness of the upper and lower layers H_1 and H_2 outside the cylinder, the initial interface displacement η_0, the reduced gravity $g' \equiv g\delta\rho/\rho$, the Coriolis parameter $f = 4\pi/T$, the viscosity ν and the diffusivity κ. By straightforward dimensional analysis, the system can be equivalently described by a time scale T and space scale R, and the following six non-dimensional parameters:

(i) The stratification parameter $\gamma = R/L_R$, where L_R is the internal Rossby radius of deformation

$$L_R = \frac{1}{f}\left(\frac{g'H_1}{1 + H_1/H_2}\right)^{1/2}.$$

Note that γ is related to the Burger number $Bu = \gamma^{-2}$.

(ii) The amplitude η_0/H_1 characterizes the sign and the intensity of the vortex. It will be seen that the vortex geostrophic velocity is of order $u \sim (\eta_0/H_1)L_R f$, so that η_0/H_1 is of the order of the Rossby number $Ro = u(fL_R)^{-1}$ based on L_R.

Name	H_1(cm)	η_0 (cm)	$\delta\rho/\rho(\times 10^{-3})$	$\gamma = R/L_R$
OO	12.5	0	1.9	2.9
C1	12.5	+2.5	2.2	2.7
A1	12.5	−5	1.1	3.8
C2	12.5	+6.25	1.4	3.4
A2	12.5	−10	1.1	3.8
A3	12.5	−12.5	1.0	4.0
C3	12.5	+12.5	1.0	4.0
C4	12.5	+12.5	1.8	3.1
A4	0	−12.5	1.7	–
A5	0	−12.5	1.7	–

TABLE 1. List of representative experiments, with their parameters. Each experiment is designated by A (anticyclone) or C (cyclone) followed by a number increasing with amplitude (OO is a test experiment with zero amplitude). The tank rotation period is 50 s in all these experiments. Additional experiments with rotation period 30 s have been used to increase the range of γ in the instability diagram of figure 11.

(iii) The thickness ratio $\delta = H_1/(H_1 + H_2)$ is here set to a constant value 1/5 (except in the case of a layer confined to the interior of the cylinder, for which $H_1 = 0$). This value is representative of oceanic situations (for example a thermocline at depth 600 m in an ocean 3000 m deep). Changing this parameter (with fixed L_R) would presumably yield only minor quantitative variations, except possibly when δ approaches the limiting values 0 or 1.

(iv) The parameter H_1/L_R is the ratio of the horizontal to vertical scales. The hydrostatic approximation is valid when this ratio is sufficiently small. In this limit, H_1/L_R has no influence on the dynamics.

(v) The Prandtl number $Pr = \nu/\kappa$. In our case, taking for κ the diffusivity of salt, $Pr = 658$, hence the effect of diffusivity can be neglected.

(vi) The Reynolds number Re based on the upper layer thickness H_1 and the typical geostrophic velocity, $Re = H_1 u/\nu = (1-\eta_0/2H_1)\eta_0 Rf(\gamma\nu)^{-1}$. In our experiments $Re \sim 1000$.

Our study is focused on the influence of γ and η_0/H_1. The parameter γ is the only relevant one in the quasi-geostrophic approximation $\eta_0/H_1 \ll 1$ (in addition to the thickness ratio $\delta = H_1/H_2$), determining the wavenumber of the baroclinic instability. In this approximation, the amplitude η_0/H_1 has no influence: it only determines the time scale of the phenomena, and reversing η_0/H_1 symmetrically changes cyclones into anticyclones.

A selection of the parameter values is indicated in table 1, for which the evolution of the velocity fields has been fully analysed. The stability properties have been explored over a wider range of parameters, γ varying from 1.8 to 4.6. This parameter was in practice determined by the relative density difference $\delta\rho/\rho$, which was varied from 1 to 5×10^{-3}, and by the tank rotation period (50 or 30 s). Below this minimum value, the stratification is difficult to control, and the radius of deformation would become smaller than the layer depth H_1, leading to non-hydrostatic dynamical regimes.

These parameter definitions are only valid in the case of an upper layer extending outside the cylinder $H_1 \neq 0$. A more general definition will be later used, see (3.8–3.9), replacing H_1 and H_2 by an estimate of the layer thickness at the edge of the vortex $H_1' = H_1 - \eta_0/2$ and $H_2' = H_2 + \eta_0/2$.

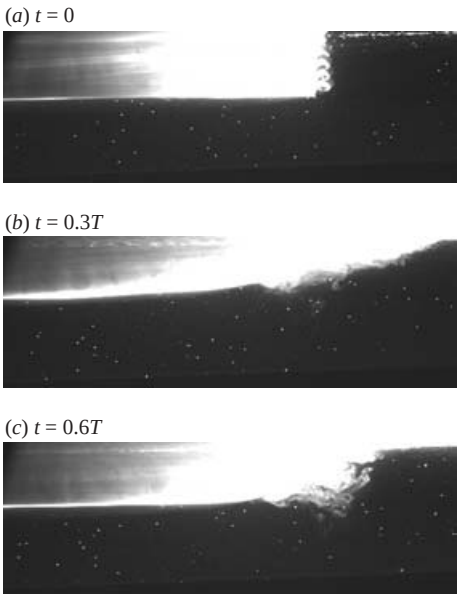

FIGURE 3. Side views of the initial oscillation. The upper layer, here initially limited to the inside of the cylinder ($\eta_0 = -12.5$ cm, $H_1 = 0$) is dyed by fluorescein and illuminated by a vertical laser sheet, crossing the cylinder along a diameter. The image is cut above at the level of the free surface, and half the vortex is visible (the initial thickness of the layer, 12.5 cm, gives the scale).

3. The balanced axisymmetric vortex

3.1. *Observation of the cyclo-geostrophic adjustment*

At the starting time $t = 0$, a radial current is driven by the radial pressure gradient in the upper layer, either outwards ($\eta_0 < 0$) or inwards ($\eta_0 > 0$). Under the effect of the Coriolis force, this current evolves into an anticyclonic ($\eta_0 < 0$), or a cyclonic ($\eta_0 > 0$) vortex, and returns backward. After a few oscillations, the radial velocity is damped, and a balanced axisymmetric vortex remains. A current of opposite sign is created in the lower layer.

These oscillations are visualized in a vertical plane as exemplified by figure 3, a case in which the upper layer is initially confined inside the cylinder. At $t = 0$, when the cylinder has just left the water surface, the shear instability left by the cylinder motion is clearly visible along the vertical edge of the layer. This is, however, a local effect, which is quickly swept away by the outward current, seen in figure 3(b). Then the flow reverses under the Coriolis effect (figure 3c).

This Coriolis effect is better seen by particle streaks in the horizontal plane, as shown in figure 4. At $t = 0$, the motion has not yet begun. The two successive views, 4(b, c), show the spiral flow due to a combination of a radial gravity current and an azimuthal motion induced by the Coriolis force.

3.2. *Prediction for the cyclo-geostrophic adjustment*

The axisymmetric state is analysed after relaxation of the inertial oscillations. The hypothesis of potential vorticity conservation provides a well-defined prediction for this adjusted state, following Rossby (1938); see also Kuo & Polvani (2000) or Stegner, Bournet-Aubertot & Pichon (2003). At time $t = 0$, the potential vorticity (PV) is uniform inside the cylinder ($r < R$), $q_1 = f/(H_1 - \eta_0)$ in the upper layer and

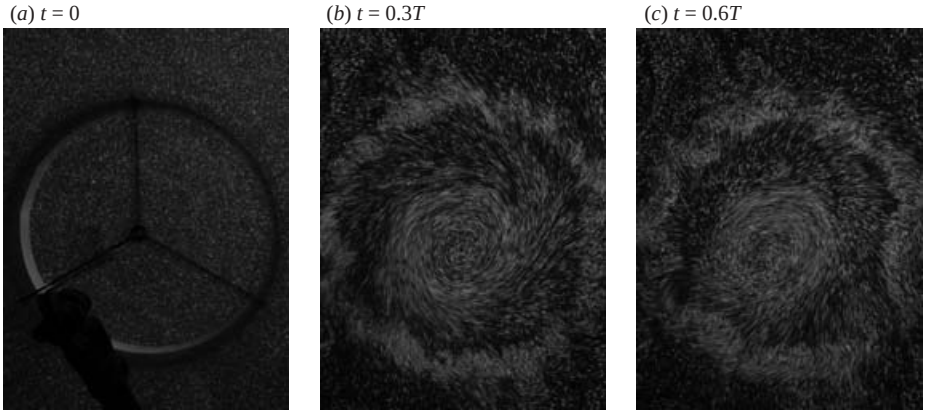

FIGURE 4. Top view of the initial oscillation, visualized by particle streaks (experiment A1, $\eta_0 = -5$ cm). The external white crown is the turbulence produced at the initial front. (*a*) Initial state the cylinder, of diameter 1 m, is visible as it has just left the free surface. (*b*) First return of the oscillation with a convergent radial current deviated by the Coriolis force. (*c*) Second phase of the divergent current.

$q_2 = f/(H_2 + \eta_0)$ in the lower one. Outside the cylinder ($r > R$), the PV is also uniform with values $q_1 = f/H_1$ and $q_2 = f/H_2$. During relaxation, the disks with uniform PV can change diameter due to the radial motion, reaching radii R_1 and R_2 respectively in both layers, but the PV values are conserved.

Using the definition of the potential vorticity, and the cyclo-geostrophic balance, exact for an axisymmetric steady inviscid flow, one obtains three equations for the velocity in the two layers $u_1(r)$ and $u_2(r)$ and the interface displacement $\eta(r)$:

$$\left(\frac{1}{r}\frac{\mathrm{d}(ru_1)}{\mathrm{d}r} + f\right)\frac{1}{H_1 - \eta} = q_1(r), \tag{3.1}$$

$$\left(\frac{1}{r}\frac{\mathrm{d}(ru_2)}{\mathrm{d}r} + f\right)\frac{1}{H_2 + \eta} = q_2(r), \tag{3.2}$$

$$\frac{\mathrm{d}\eta}{\mathrm{d}r} = -\frac{1}{g'}\left[f(u_1 - u_2) + \frac{u_1^2}{r} - \frac{u_2^2}{r}\right]. \tag{3.3}$$

These are solved by a shooting method, in terms of the functions u_1/r, u_2/r, and η. The condition $\eta = 0$ at large radius r is used, and in the limit $r \to 0$, u_1/r is equal to half the vorticity ζ_1, expressed in terms of the PV, $u_1/r = \zeta_1/2 = ((H_1 - \eta)q_1 - f)/2$. Similarly, one can prescribe $u_2/r = \zeta_2/2 = ((H_2 + \eta)q_2 - f)/2$ for $r = 0$. The unknown radii R_1 and R_2 for the uniform-PV disks are implicitly determined by the conditions of volume conservation for each PV patch:

$$\int_0^{R_1} (H_1 - \eta) r \, \mathrm{d}r = R^2(H_1 - \eta_0)/2, \tag{3.4}$$

$$\int_0^{R_2} (H_2 + \eta) r \, \mathrm{d}r = R^2(H_2 + \eta_0)/2. \tag{3.5}$$

Predicted velocity fields are plotted in figure 5 (curves CG) where they are also compared with experimental results. The extremum velocity is obtained at $r = R_1$ in the upper layer and $r = R_2$ in the lower layer. For cyclones, $R_1 < R$ and $R_2 > R$. This

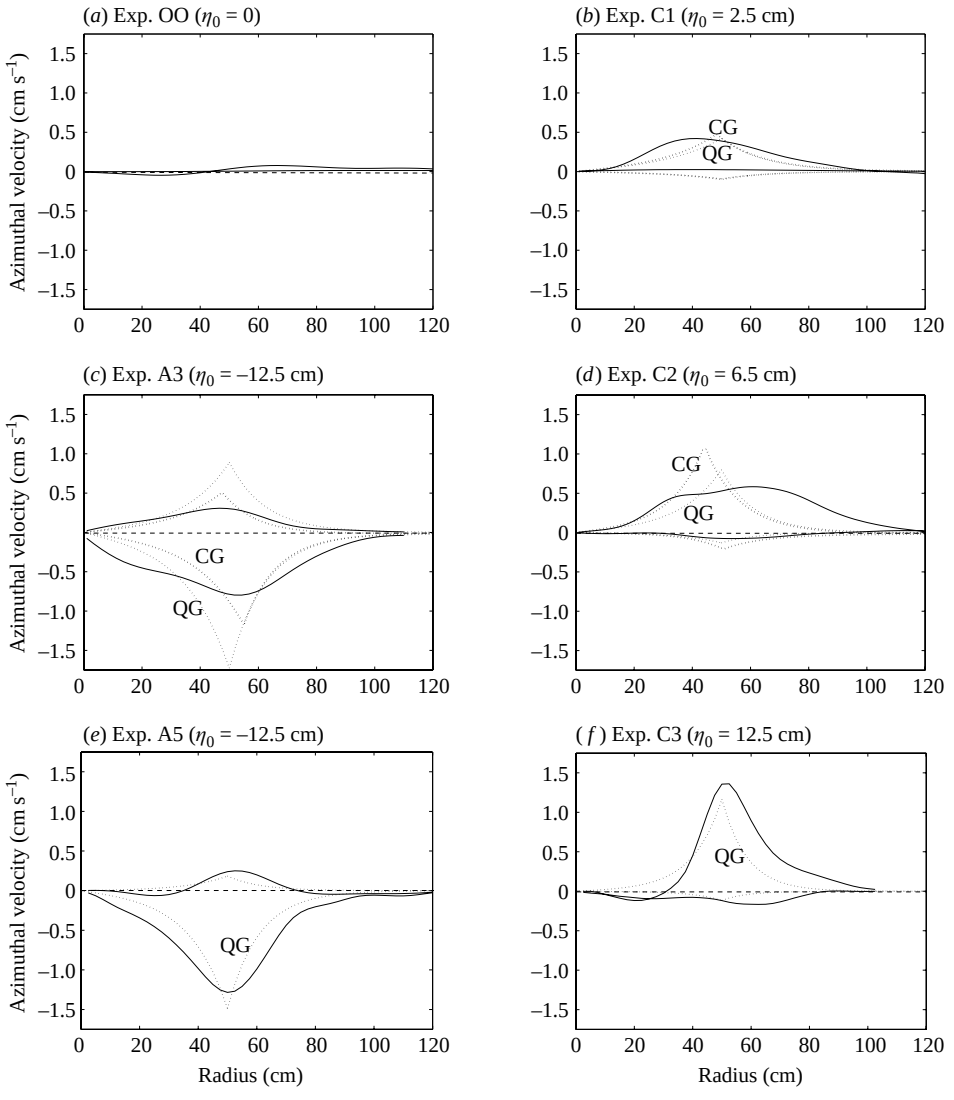

FIGURE 5. Azimuthal velocity versus radius for the balanced vortex with different initial amplitudes η_0. For each layer, the measured profiles (averaged over the azimuth and on the time interval [$2T$ to $3T$]) are plotted as solid lines, the cyclo-geostrophic (CG) prediction (3.1)–(3.3) as thick dashed lines and the quasi-geostrophic (QG) prediction (3.6) as thin dashed (in *e* and *f* the numerical scheme did not yield the CG result as the layer is interrupted).

case corresponds to $\eta_0 > 0$ and during the adjustment process, the water mass inside the cylinder radially contracts in the upper layer and spreads in the lower layer. The opposite is predicted for anticyclonic vortices.

3.3. *Comparison with measurements*

The azimuthal velocity profile is measured after the relaxation of the inertial oscillations and before the growth of the baroclinic instability, which is possible as the time scales are clearly separated. In practice we average the velocity fields in the time interval $2T$ to $3T$ to eliminate residual oscillations. Then we azimuthally average the azimuthal velocity component around the vortex.

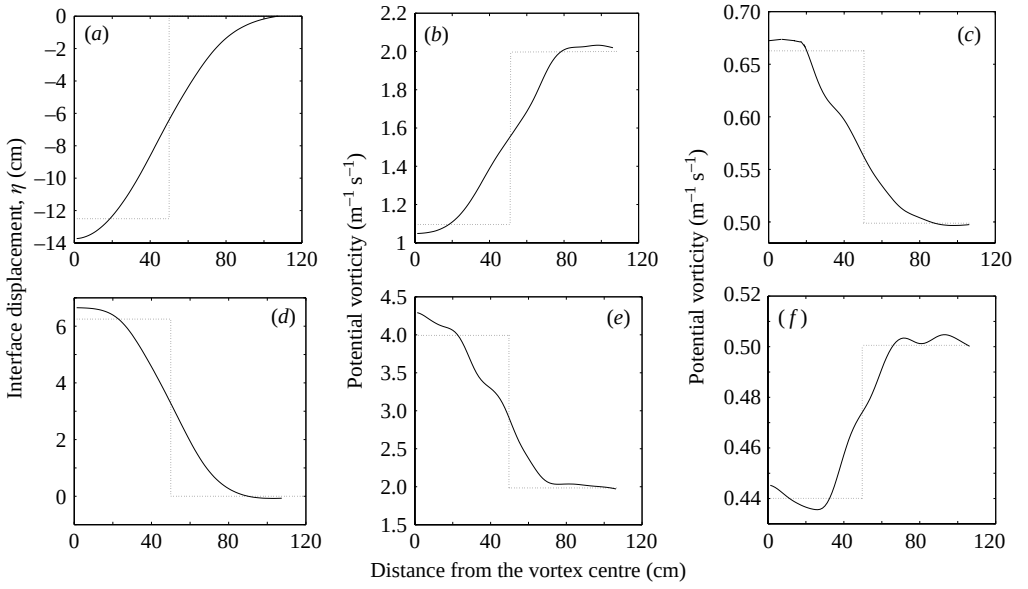

FIGURE 6. Interface displacement (a, d) and potential vorticity ((b, e) in the upper layer and (c, f) in the lower layer) for experiment A3 ($\eta_0 = -12.5$ cm) (a–c) and experiment C2 ($\eta_0 = 6.25$ cm) (d–f) versus the distance from the centre (in cm). The solid lines are calculated for the time corresponding to the geostrophic adjustment and the dotted lines represent the initial values.

A reasonable agreement between the experimental results and the predictions is observed, see figure 5. In particular, in the standard cases (5c, d), an opposite velocity is found in the upper and lower layer, roughly in inverse proportion to the respective layer thickness. Systematic discrepancies to the inviscid two-layer predictions are observed however: the velocity profile is somewhat broadened, with a maximum velocity lower than predicted.

This broadening can be interpreted in terms of PV mixing. Examples of measured PV profiles are represented in figure 6 for a cyclone (C2) and an anticyclone (A3). These results have been deduced from the velocity profiles measured in each layer, using (3.1) and (3.2), where the interface displacement $\eta(r)$ has been obtained by (3.3). The theoretical PV profile, in the absence of mixing, is also represented by dotted lines. The two initial values are preserved within the experimental uncertainty at the vortex centre and at large radii. The initial discontinuity in the PV profile has been smoothed out however, as expected from PV mixing.

This mixing effect can be quantified for instance by the difference between the predicted velocity extremum and the measured one (see table 2 below). The discrepancy seems consistently stronger for low amplitude η_0. A reason for this result may be that the geostrophic velocity scales like η_0, while the speed of the initial radial current scales like $|\eta_0|^{1/2}$, so that the influence of the latter is expected to increase with lower amplitude η_0. Note however that the amount of PV mixing is not quite reproducible; the extremum velocity varies by about $\pm 15\,\%$ when an experiment is repeated (compare for instance the maximum velocity measured in experiments A4 and A5, table 2). This may be associated with the transient development of short-scale instabilities, as visualized in figure 4. Such transients are quickly damped in the adjusted axisymmetric state, before the growth of the slower baroclinic instability. To

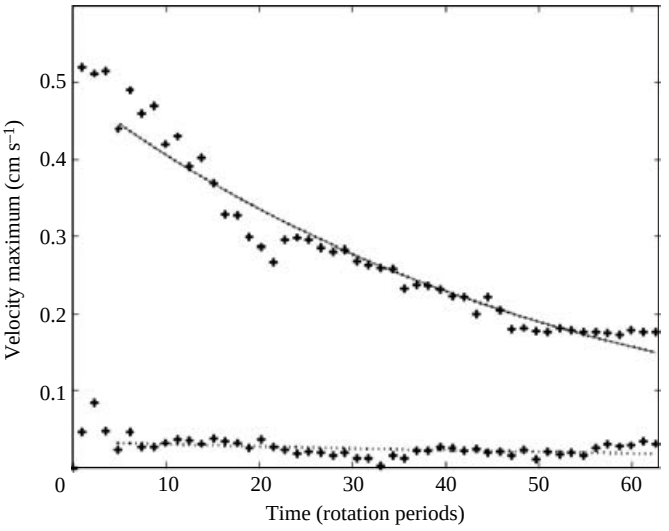

FIGURE 7. Decay of the maximum velocity versus time in the upper and lower layer for a stable vortex (1 field/minute). A fit with exponential decay is indicated (experiment C1).

test the possibility of spurious mixing induced by the wake of the cylinder, or by the spray used for particle seeding, we have performed a test case with $\eta_0 = 0$ (run OO). Negligible motion is obtained (figure 5*a*), so that PV mixing is in fact associated with the cyclo-geostrophic adjustment.

In summary, the vortices are found to reach a steady balanced state within 2–3 tank rotation periods. The PV is extremum at the vortex centre with a constant sign gradient, which is opposite in the two layers. This is a necessary condition for baroclinic instability (Charney & Stern 1962).

This balanced state decays only very slowly with time through viscous effects. This can be checked by measuring the velocity decay in a stable case, as shown in figure 7. The maximum velocity modulus, rather than the azimuthally averaged velocity, has been plotted to take into account the existence of a slow residual motion of the vortex centre. After the fast damping of the inertio-gravity waves, i.e. for $t > 5T$, an exponential decay $\exp(-0.4 \times 10^{-3} t)$ is found for the upper layer. Note that it is about 8 times less than the Ekman decay rate $(\nu f/2)^{1/2}/H_1$ which would occur for a layer with the same thickness H_1 over a rigid bottom. This measured decay rate is about 10 times less than the typical growth rate obtained for the baroclinic instability, so that bottom friction has a negligible influence.

3.4. *An effective quasi-geostrophic model*

In the quasi-geostrophic (QG) limit ($\eta_0/H_1 \to 0$), the balance equations (3.1)–(3.3) have an explicit solution. The horizontal velocity then has zero divergence, so that the PV disks keep their initial area, $R_1 = R_2 = R$. The PV values inside this disk are approximated as $q_1 H_1/f = 1 + \eta_0/H_1$ and $q_2 H_2/f = 1 - \eta_0/H_2$ respectively in each layer. The velocity field is then purely baroclinic, $H_1 U_1 + H_2 U_2 = 0$, so that each velocity is expressed in terms of the baroclinic component $U_1 - U_2$ and the thickness ratio $\delta = H_1/(H_1+H_2)$: $U_1 = (1-\delta)(U_1-U_2)$ and $U_2 = -\delta(U_1-U_2)$. The displacement η is a solution of the axisymmetric Helmholtz equation $-\Delta\eta + \eta/L_R^2 = \eta_0/L_R^2$ inside the disk,

Name	δ'	γ'	$\eta_0/2H_1'$	V_1exp	V_1CG	V_1QG	V_2 exp	V_2(CG)	V_2(QG)
OO	0.2	2.9	0	+0.07	0	0	0.01	0	0
C1	0.18	2.8	0.11	+0.45	+0.48	+0.42	0.03	−0.10	−0.09
A1	0.25	3.6	−0.17	−0.58	−0.56	−0.68	0.12	0.17	+0.23
C2	0.14	3.8	+0.33	+0.61	+1.12	+0.80	−0.15	−0.19	−0.13
A2	0.31	3.4	−0.29	−0.97	−0.88	−1.42	+0.44	+0.38	+0.64
A3	0.34	3.5	−0.33	−0.78	−1.25	−1.73	+0.38	+0.50	+0.90
C3	0.09	5.3	+1	+1.38	–	+1.16	−0.18	–	−0.11
C4	0.09	4.1	+1	+1.93	–	+1.48	–	–	−0.14
A4	0.11	4.1	−1	−1.70	–	−1.49	–	–	0.18
A5	0.11	4.1	−1	−1.35	–	−1.49	+0.25	–	0.18

TABLE 2. Modified parameters δ' and γ' given by (3.9) and (3.8), and extremum equilibrium velocity measured in both layers (V_1 exp and V_2 exp) compared to the cyclo-geostrophic predictions CG (3.1)–(3.3) and the quasi-geostrophic predictions QG (3.6). The list of representative experiments of table 1 is used.

and $-\Delta\eta+\eta/L_R^2 = 0$ outside. The resulting baroclinic velocity $U_1-U_2 = -(g'/f)\mathrm{d}\eta/\mathrm{d}r$ is

$$U_1 - U_2 = V(\gamma) \begin{cases} I_1(\gamma r/R)/I_1(\gamma) & \text{if } r < R, \\ K_1(\gamma r/R)/K_1(\gamma) & \text{if } r \geqslant R, \end{cases} \tag{3.6}$$

$$V(\gamma) = \frac{\eta_0}{H_1}\frac{Rf}{(1-\delta)}\frac{1}{\gamma}\left(\frac{K_0(\gamma)}{K_1(\gamma)} + \frac{I_0(\gamma)}{I_1(\gamma)}\right)^{-1}, \tag{3.7}$$

where I_0, I_1, K_0, K_1 are the modified Bessel functions of zero and first order. For large γ, the velocity is increasingly confined to the disk edge, forming a jet of width $1/\gamma$ and a maximum baroclinic velocity $V(\gamma) \simeq (\eta_0/H_1)L_R f[2(1-\delta)]^{-1}$ (this limit has already been reached within 5 % for $\gamma = 3$).

These analytical results provide a convenient approximation to the true cyclo-geostrophic profiles. The velocity is overestimated for large amplitudes η_0/H_1 however. The approximation can be improved by taking the reference interface position at the middle of the initial step, instead of the equilibrium position at large distance r. This means replacing H_1 and H_2 by the modified reference layer thickness $H_1' = H_1 - \eta_0/2$ and $H_2' = H_2 + \eta_0/2$. Then the stratification parameter γ and layer thickness ratio δ are replaced respectively by the effective parameters

$$\gamma' = \gamma^2\left[\left(1-\frac{\eta_0}{2H_1}\right)\left(1+\frac{\eta_0}{2H_1}\frac{\delta}{1-\delta}\right)\right]^{-1}, \tag{3.8}$$

$$\delta' = \frac{1-\dfrac{\eta_0}{2H_1}}{1+\dfrac{\eta_0}{2H_1}\dfrac{\delta}{1-\delta}}. \tag{3.9}$$

In the limiting case of an outcroping interface, with initially no upper layer outside the cylinder, γ is not defined, since $H_1 = 0$. By contrast this modified formulation provides a well-defined quasi-geostrophic model, with $H_1' = |\eta_0|/2$ and $H_2' = H - |\eta_0|/2$. Then the relative amplitude $\eta_0/(2H_1')$ is always in the interval $[-1, 1]$. Values of these effective parameters are given in table 2, as well as the corresponding predicted QG extremum velocities. Some QG velocity profiles are plotted in figure 5.

4. Initial growth of the instability

4.1. *Predictions of linear stability*

The PV profile of our vortex is monotonic in each layer, so it is barotropically stable: the instability is genuinely baroclinic, associated with the vertical shear. The simplest approach is then the quasi-geostrophic model by Phillips (1954): the unperturbed velocity is assumed uniform in each layer, with values U_1 and U_2 respectively. For convenience the flow is considered in a channel along the x-coordinate, laterally confined between $y=0$ and $y=R$, so that the perturbation varies as $\mathrm{e}^{\mathrm{i}k(x-ct)}\sin ly$. The growth rate $\sigma \equiv kc_i$ and propagation speed c_r are given as the imaginary and real parts of the dispersion relation:

$$c = \frac{(U_1 - U_2)}{2(1+\gamma^2/K^2R^2)}[(1-2\delta) \pm \sqrt{1-4\delta(1-\delta)\gamma^4/K^4R^4}] \tag{4.1}$$

where K is the wave-vector modulus, $K^2 = k^2 + l^2$. Instability occurs when the argument under the square root becomes negative. Following Griffiths & Linden (1981*a*), this model can be empirically matched to our circular vortex, by unwrapping the circle $r=R$. We assume $l=0$ for simplicity, so the confinement by the channel is not relevant. Then $k=K$ and $KR=n$ are set by the angular mode number n.

A more precise model is provided by a stability analysis for a circular vortex, idealized as a disk of uniform PV, with the quasi-geostrophic velocity (3.6). The disk contour is deformed by a perturbation in $\mathrm{e}^{\mathrm{i}n(\theta-ct/R)}$ in the upper layer (and $\mathrm{e}^{\mathrm{i}[n(\theta-ct/R)-\phi_{2-1}]}$ in the lower layer). This induces a velocity perturbation which is a solution of the Helmholtz equation $-\Delta\eta + \eta/L_R^2 = 0$ inside and outside the disk, and the matching condition yields the dispersion relation (see Sokolovskiy & Verron 2000)

$$c = \frac{V}{2}\left(1 - \frac{L_n(\gamma)}{L_1(\gamma)}\right)\left[(1-2\delta) \pm \sqrt{1-4\delta(1-\delta)\frac{1/(2n)-L_n(\gamma)}{L_1(\gamma)-L_n(\gamma)}}\right] \tag{4.2}$$

where V is the maximum baroclinic velocity (at radius $r=R$), given by (3.6), and $L_n(\gamma) \equiv I_n(\gamma)K_n(\gamma)$ (note that $L_n(\gamma)$ is a decreasing function of n and tends to $1/(2\gamma)$ for large n, so that $L_1(\gamma) - L_n(\gamma) > 0$ and $1/(2n) - L_n(\gamma) > 0$).

The corresponding growth rate $\sigma = n\ \mathrm{Im}(c/R)$ is plotted in figure 8 versus γ. Notes that the first unstable mode is $n=2$ (a perturbation with $n=1$ just corresponds to a small shift in the vortex position). This result is close to Phillips' model, provided one takes an effective velocity $U_1 - U_2 \simeq V/2$ (and the choice of a purely longitudinal wave-vector, $l=0$, which provides the best correspondence). For large values of γ, the vortex flow takes the form of a circular jet, with a non-uniform velocity (the jet width L_R is of the order of the most unstable wavelength). Therefore we cannot justify this correspondence as an asymptotic limit. It provides a convenient fit however, valid for a wide range of thickness ratios δ.

The rotation speed $c_r/R = \mathrm{Re}(c)/R$ of the perturbation is plotted in figure 9. The results for the vortex are again in good agreement with Phillips' model with $U_1 - U_2 = V/2$. The perturbation is advected by the fastest (upper) layer, but at about 5 % of the maximum fluid velocity $(1-\delta)V$ in this layer.

For Phillips' model, each mode n becomes unstable when $\gamma = n[4\delta(1-\delta)]^{-1/4}$, and is most amplified when $\gamma \simeq 1.5n[4\delta(1-\delta)]^{-1/4}$; the most amplified perturbation wavelength scales as L_R. For this most amplified wavenumber, the dispersion relation

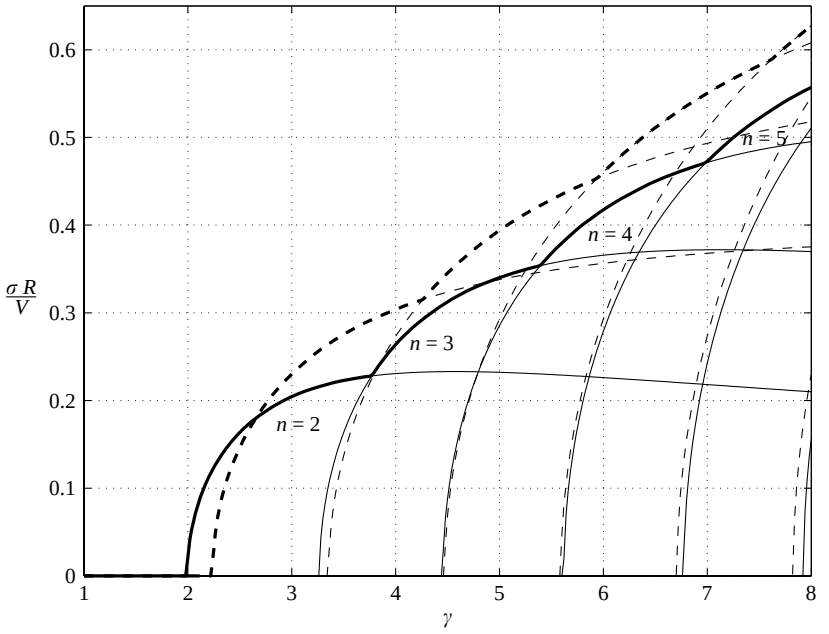

FIGURE 8. Growth rate $n\,\mathrm{Im}(c)$ versus γ, predicted for perturbations with angular mode n on a disk of uniform PV relation (4.2) (solid lines) and for the equivalent Phillips model relation (4.1) with $U_1 - U_2 = V/2$ (dashed line). The bold part of the curves corresponds to the mode with the maximum growth rate.

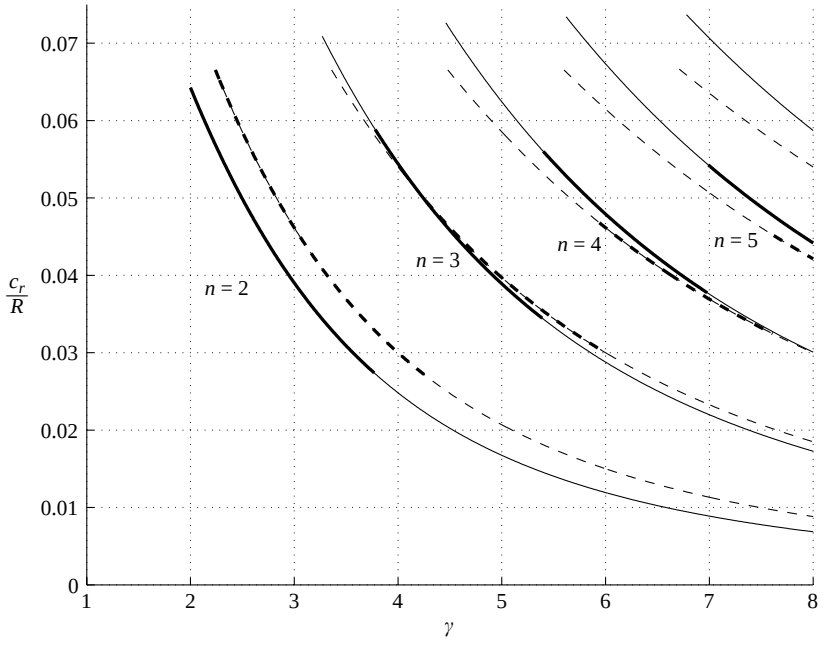

FIGURE 9. Angular propagation speed versus γ predicted for the amplified perturbations on a disk of uniform PV real part of (4.2) (solid line), and for the equivalent Phillips model real part of (4.1) with $U_1 - U_2 = V/2$ (dashed line). The bold part of the curves corresponds to the mode with the maximum growth rate.

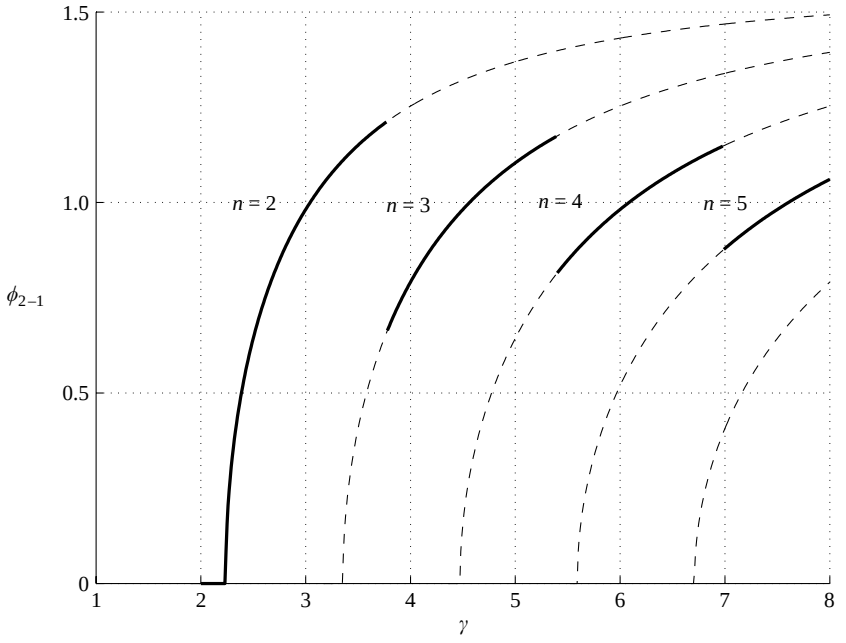

FIGURE 10. Phase difference versus γ predicted for perturbations with angular mode n on a disk of uniform PV relation (4.2) (solid lines), and for the equivalent Phillips model relation (4.1) with $U_1 - U_2 = V/2$ (dashed line). The bold part of the curves corresponds to the mode with the maximum growth rate.

(4.1), with $U_1 - U_2 = V/2$, can be approximated as

$$\frac{c}{V} \simeq \frac{[\delta(1-\delta)]^{1/2}}{1 + 1.6[\delta(1-\delta)]^{1/2}}[0.4(1-2\delta) + 0.5\mathrm{i}] \tag{4.3}$$

which provides a convenient practical estimate. For our experiments ($\delta = 0.2$), this yields $c_r/V = 0.05$ and $c_i/V = 0.12$ (so that $\sigma = 0.12\, nV/R$).

The phase difference for the perturbations in the two layers is also an interesting prediction of the theory. For Phillips' model, it is given by (see e.g. Pedlosky 1979)

$$\tan\phi_{2-1} = \frac{c_i(U_1 - U_2)}{|c - U_2|^2\,(K^2/\delta\gamma^2 + 1) - (U_1 - U_2)(c_r - U_2)}. \tag{4.4}$$

This predicted phase difference is represented in figure 10. For the most amplified mode, this phase is always close to 1 rad (except close to the threshold of instability). This result is obtained for any thickness ratio δ, and can be considered as a signature of the baroclinic instability. This is not very far from the value $\pi/4$ obtained by the argument of Bretherton (1966) and Hoskins, McIntyre & Robertson (1985). The perturbation is then sketched as a chain of vortices (PV anomalies). For a phase shift of $\pi/4$ between the two layers, each vortex in a layer induces a transverse velocity in the other layer which amplifies its transverse displacement. This phase difference therefore indicates an active interaction between the two layers. By contrast, the vortex dynamics is controlled mainly by the upper layer which produces a passive footprint on the lower layer, with the same or opposite phase as the upper layer. This would be the case for a barotropic instability.

These models rely on the hydrostatic approximation for shallow layers, assuming a velocity independent of depth in each layer. This could be a critical issue for the thick lower layer. In reality the perturbation propagates in this layer as an inertial (gyroscopic) wave, with dispersion relationship $\omega/f = \pm k_z/|\boldsymbol{k}|$. For the baroclinic instability $|\omega| \ll f$, so that $\boldsymbol{k}$ is dominated by its horizontal component $k = n/R$, and $k_z \simeq (n/R)(\omega/f)$. Using our practical estimate (4.3) for the most amplified mode, with our previous estimate for the QG velocity V, we obtain

$$k_z H_2 \simeq (1-\delta)\frac{\eta_0}{L_R}\frac{0.4 \pm 0.32(1-2\delta)\mathrm{i}}{1+1.6[\delta(1-\delta)]^{1/2}}$$

(it must have both real and imaginary components, as $\omega = -kc$ is complex). In our case $\delta = 0.2$, it is found that $k_z H_2 \simeq 0.2 \pm 0.2\mathrm{i}$ in the extreme case of an initial displacement η_0 equal to the radius of deformation L_R). Therefore $k_z H_2 \ll 1$, so that the horizontal velocity in each layer can be considered as independent of z: in other words the hydrostatic approximation remains quite good in describing the baroclinic instability, although the layer thickness is comparable to the horizontal scale.

4.2. *Experimental results*

After the geostrophic adjustment into an axisymmetric flow, the progressive folding of the vortex contour and its splitting into n secondary vortices is observed. This instability develops when the parameter γ is greater than about 2.5. The stability properties for a series of experiments with different stratification γ and amplitude η_0/H_1 are indicated in figure 11(*a*). Examples are visualized in figure 11(*b–d*). A dominant wavenumber $n = 2$ is observed approximately in the range $2.5 < \gamma < 3.5$, and $n = 3$ until $\gamma \simeq 5$, the maximum value explored in our experiments.

These results are in reasonable agreement with the stability theory in the QG model. The predicted threshold from (4.2) is indeed $\gamma = 2.0$ for the onset of the first mode $n = 2$, and the mode $n = 3$ should dominate from $\gamma = 3.8$ to 5.4. The observed crossover between $n = 2$ and 3 is therefore in good agreement with the theory. The observed threshold for the onset of the first instability at $n = 2$ is a little higher than the prediction, but the expected slow growth is difficult to detect and it is sensitive to background residual flows.

We find remarkable that these thresholds do not depend much on the amplitude η_0/H_1, so the QG results apply well even for the extreme cases, for instance at $\eta_0/H_1 = 1$ for which the upper layer is interrupted in the vortex core. There is, however, a small shift of both thresholds to smaller γ when η_0/H_1 approaches 1. This trend is confirmed by our direct numerical simulations. It can be explained in the framework of the QG model by the simple argument on the choice of the unperturbed layer thickness, discussed at the end of § 3.2. Applying the QG model to the transformed parameters γ' and δ' given by (3.8) and (3.9), one finds the mode boundaries plotted in figure 11(*a*). For the extreme case of an upper layer confined to the inside of the vortex (not represented in figure 11*a*), these effective parameters are $\delta' = 0.11$ and $\gamma' = 4.1$. The predicted dominant mode is then $n = 3$, in agreement with the observations.

A quantitative analysis of the instability is performed by a Fourier analysis of the radial velocity component u_r along a circle. We choose the circle at radius $r = R$ for which the perturbation is maximum: the amplitude and phase of the perturbation mode n in each layer are calculated from

$$\widehat{A}_n = \frac{1}{\pi}\int_0^{2\pi} u_r(R,\theta)\exp(\mathrm{i}n\theta)\,\mathrm{d}\theta.$$

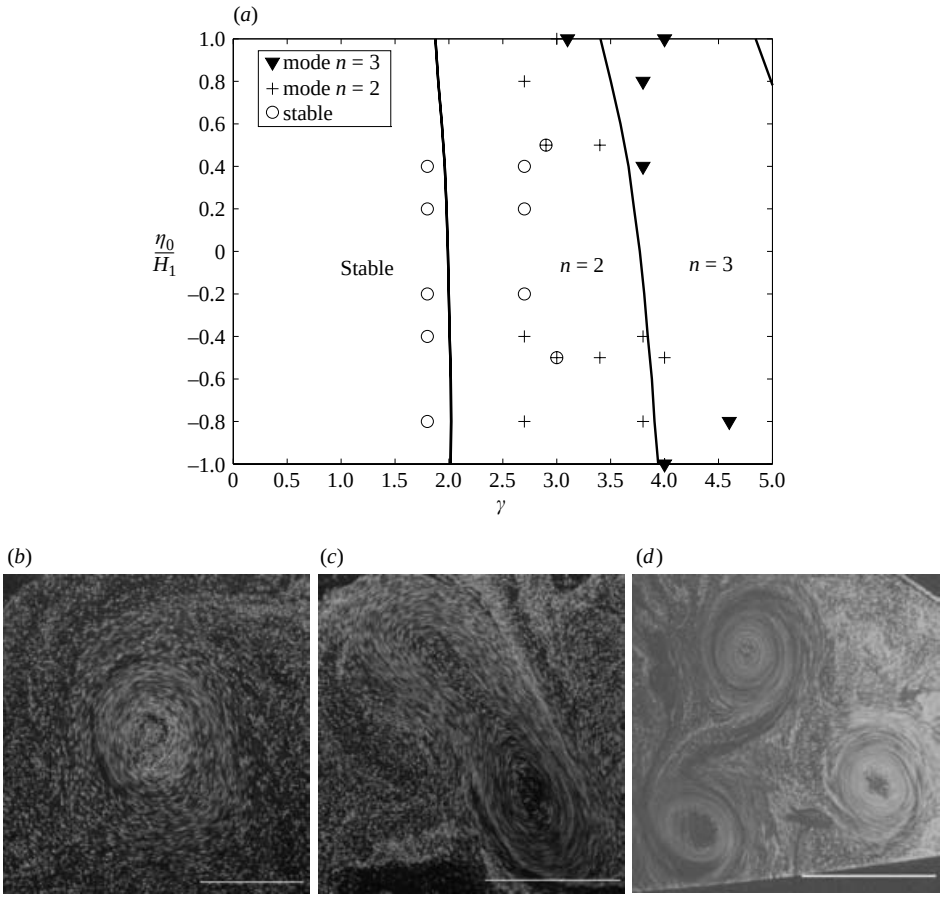

FIGURE 11. (*a*) Diagram summarizing the observations of stable vortices, splitting with mode $n=2$, splitting with mode $n=3$. The prediction of stability boundary for the mode $n=2$, and the domain of dominance of the mode $n=3$, are indicated by the solid lines. The predictions are made from the QG model (4.2) with the effective parameters (3.8)–(3.9). (*b*) Example of stable vortex (C1) (*c*), vortex splitting with mode $n=2$ (A2) (*d*) vortex splitting with mode $n=3$ (C4), visualized by particle streaks in the upper layer (the white line gives the scale 1 m). The streak photos are taken at $t=15T$ (tank periods) after the cylinder lift.

For a perturbation $u_0\cos[n\theta-\phi]$, this yields $\widehat{A}_n = u_0\exp \mathrm{i}\phi$, so the mode amplitude and its phase ϕ are obtained respectively as the modulus and argument of $\widehat{A}_n$.

An example is shown in figure 12 for modes $n=2$ and 3. The amplitude of the mode $n=1$ would correspond to a shift of the vortex and we check that it is close to zero, indicating that the vortex remains centred on the same origin.

We observe first the growth of instability in both layers up to a maximum. At this stage, the vortex splits so the amplitude drops, as there is no longer velocity at the radius $r=R$. During the time of perturbation growth, the phase varies monotonically, indicating a steady rotation of the perturbation. The direction of this rotation is set by the direction of the vortex in the upper layer. In the example of figure 12, the vortex is anticyclonic, so the phase decreases versus time. The same phase difference $|\phi_{2-1}|=1\pm0.2$ rad between the two layers is observed in all the experiments. It is a very robust property, persisting far into the nonlinear regime. The sign of ϕ_{2-1}

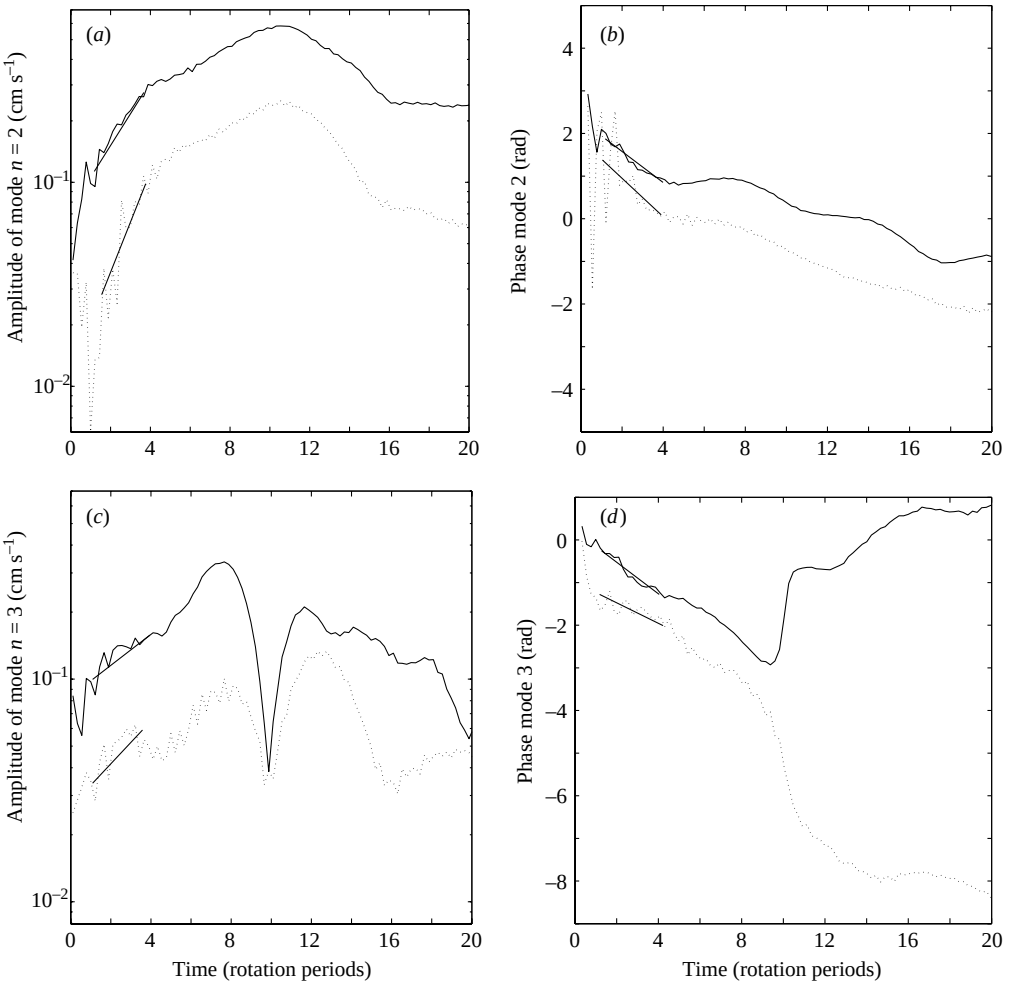

FIGURE 12. Amplitude (a, c) and phase (b, d) versus time of the azimuthal modes $n = 2$ (a, b) and $n = 3$ (c, d). The perturbation in radial velocity in the upper layer (solid line) and lower layer (dotted line) is analysed (experiment A3: $\eta_0 = -12.5$ cm, $\gamma = 4.0$).

reverses for a reversed vortex sign, such that the perturbation in the upper layer always lags the perturbation in the lower layer.

We have checked that the perturbations are independent of depth inside the lower layer, which supports the description of the system in terms of a two-layer model. The perturbation amplitude and phase at different levels in the lower layer do indeed coincide well, see figure 13, after a phase of adjustment of a few tank rotation periods. This confirms the argument at the end of § 4.1.

The development of the instability is best visualized in terms of PV fields, as shown in figure 14. We obtain PV from the experimental velocity fields by the method of data assimilation presented in § 2.3. Here we define the PV in each layer as $q_1 - f/H_1$ and $q_2 - f/H_2$, subtracting the far-field values. The initial condition is to a good approximation a patch of uniform PV in the upper layer (here negative) and a corresponding disk of opposite PV in the lower layer. Initial perturbations can be seen as small vortices around the main vortex: these have been formed mostly

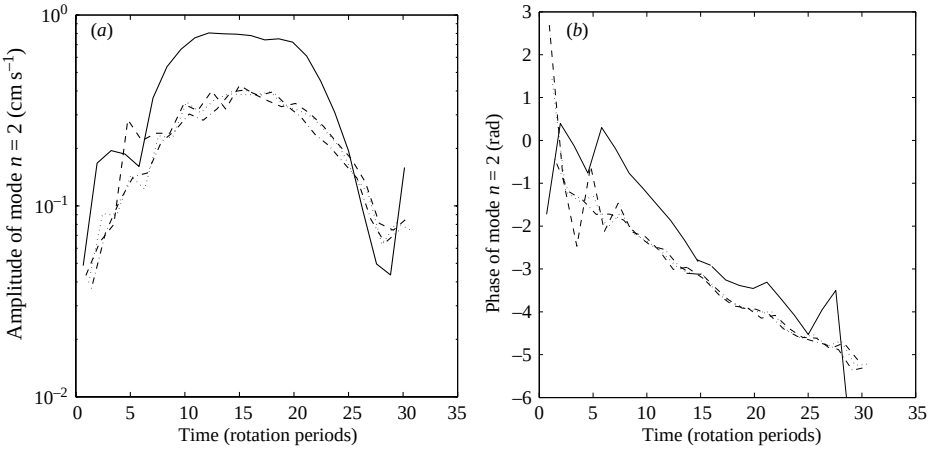

FIGURE 13. Amplitude (a) and phase (b) of the perturbations in the upper layer represented with a solid line ($z = 6.25$ cm) and at three levels in the lower layer represented with broken lines ($z = 18.75$, 31.25, 43.75 cm) for experiment A2.

by water droplets during the particle seeding of the upper layer. The instability appears as a deformation of each PV disk, locked in phase in both layers. This pattern slowly rotates in the same direction (here anticyclonic) as the upper layer. In this case a mixture of modes $n = 3$ and $n = 2$ initially grows, but the mode $n = 2$ eventually dominates. Note that since the basic PV patch is negative in the upper layer, an outward contour displacement locally corresponds to a negative PV anomaly. Therefore the radial contour displacement is of opposite phase to the PV perturbation. By contrast, the PV patch is positive in the lower layer, so the radial contour displacement there is in phase with the perturbation. Therefore the contour deformation rotates in advance in the upper layer with respect to the lower layer, with a phase difference $\phi_{2-1} - \pi \simeq -2$ rad, while the velocity and PV perturbation lag in the upper layer with the phase difference $\phi_{2-1} \simeq 1$ rad, as discussed above.

4.3. *Quantitative comparison with stability theory*

Measured values of the growth rate, rotation speed and phase difference are given in tables 3 and 4 for modes $n = 2$ and 3 respectively. To get objective measures, we make a linear fit for the amplitude logarithm and for the phases over the appropriate time interval. This time interval must begin when the perturbation has already emerged well from the initial noise, and ends when nonlinear effects become significant. We observe that the growth rate begins to decrease when the mode amplitude in the upper layer exceeds about 0.4 of the maximum of the tangential velocity modulus u_θ in this layer (this corresponds to a maximum perturbation slope $u_r/u_\theta = 0.4$). To safely avoid initial noise effects, an initial perturbation larger than $0.12\max(u_\theta)$ is required. We therefore analyse the mode properties in the time interval for which the upper-layer perturbation amplitude is between $0.12\max(u_\theta)$ and $0.4\max(u_\theta)$. The corresponding fits are indicated in figure 12. When a mode amplitude does not reach $0.12\max(u_\theta)$, the mode is considered to be stable.

The growth rates measured in the two layers are indicated as σ_1 and σ_2 in tables 3 and 4. The precision of these measurements can be estimated as $\pm 2 \times 10^{-3}\,\mathrm{s}^{-1}$: growth rates smaller than this value are not detected and are set equal to 0. For a well-developed perturbation the growth rate in each layer should be the same, and this is

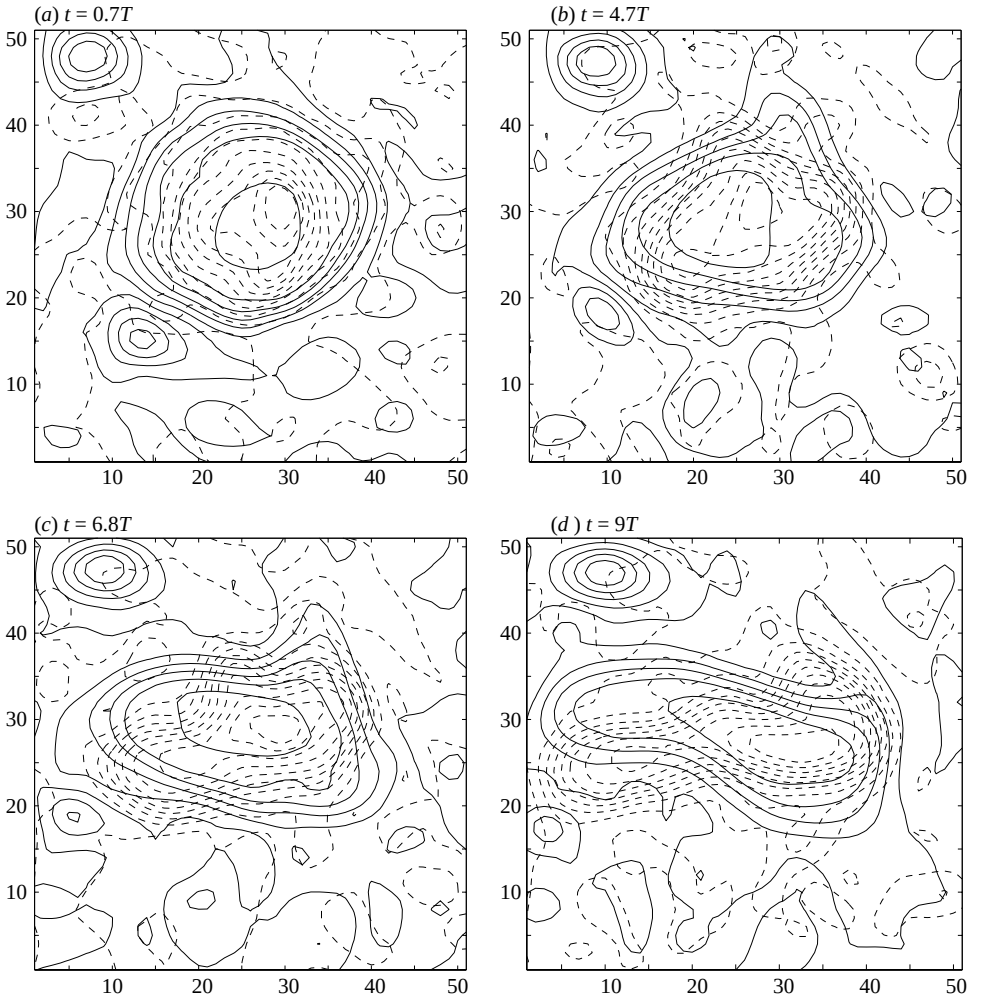

FIGURE 14. Potential vorticity anomaly in the upper (solid line) and lower layer (dashed line) for experiment A3 ($\eta_0 = -12.5\,\mathrm{cm}$, $\gamma = 4.0$) at successive times during the growth of the baroclinic instability. The iso-values are from -0.11 to 0.16 $f/H_1$with interval 0.03 f/H_1 in the upper layer, and from -0.02 to 0.11 f/H_2 with interval 0.015 f/H_2 in the lower layer. The unit on axis is the grid mesh, equal to 5 cm (used for both computations and PIV measurements).

satisfied, taking into account this margin of error. The agreement with the theoretical prediction σ_{th} is within a factor of two, which is also the quality of prediction of the maximum velocity in the vortex. These QG predictions seem consistently smaller than the experiments by a factor of 2 in the case of strong cyclones ($\eta_0/H_1 \to 1$), see experiments C3, C4, C2 in tables 3 and 4, while there is no systematic trend for anticyclones.

The angular speed of the perturbations $(1/n)\,\mathrm{d}\phi_1/\mathrm{d}t$, obtained from the perturbation phase ϕ_1 measured in the upper layer, is also given in these tables. A similar result would be obtained from the lower layer, as the phase difference ϕ_{2-1} remains constant. As expected, the perturbation always rotates in the direction of the upper-layer vortex, but at a rate systematically higher than the theoretical prediction $(1/n)\,\mathrm{d}\phi_{th}/\mathrm{d}t$. This prediction is obtained for a purely baroclinic vortex however, while velocity

Name	$\eta_0/2H_1'$	σ_1	σ_2	σ_{th}	$(1/2)\,\mathrm{d}\phi_1/\mathrm{d}t$	$(1/2)\,\mathrm{d}\phi_{th}/\mathrm{d}t$	ϕ_{2-1}
OO	0	0	0	0	–	–	–
C1	0.11	0	0	2	–	+0.5	–
A1	−0.17	4	3	5	−2	−0.5	1.2
C2	+0.33	10	8	4	+3.5	+0.6	1.1
A2	−0.29	4	7	11	−3.5	−0.8	1.1
A3	−0.33	5	7	14	−2.5	−0.9	1.0
C3	+1	0	0	4	–	+0.5	–
C4	+1	10	–	5	+3.5	+1.0	–
A4	−1	5	–	6	−2.5	−1.0	–
A5	−1	5	8	6	−2	−1.0	1.1

TABLE 3. Growth rates σ_1 and σ_2 (units $10^{-3}\,\mathrm{s}^{-1}$) for the mode $n=2$, measured in layer 1 and 2 respectively, compared to the theoretical prediction σ_{th}. The measured angular speed (unit 10^{-3} rad s^{-1} of the perturbation $(1/2)\,\mathrm{d}\phi_1/\mathrm{d}t$ is also compared to the prediction $(1/2)\,\mathrm{d}\phi_1/\mathrm{d}t$. Finally the measured phase difference ϕ_{2-1} between the top and bottom layers is indicated. The list of representative experiments of table 1 is used.

Name	$\eta_0/2H_1'$	σ_1	σ_2	σ_{th}	$(1/3)\,\mathrm{d}\phi_1/\mathrm{d}t$	$(1/3)\,\mathrm{d}\phi_{th}/\mathrm{d}t$	ϕ_{2-1}
OO	0	0	0	0	–	–	–
C1	+0.11	0	0	0	–	–	–
A1	−0.17	3	5	4	−2	−1.0	0.9
C2	+0.33	0	0	3	–	+1.3	–
A2	−0.29	0	0	10	–	−1.8	–
A3	−0.33	6	8	15	−2.7	−1.8	1.0
C3	+1	9	10	5.5	+3	+1.2	0.8
C4	+1	14	–	2.6	+3.3	+2.3	–
A4	−1	6	–	5	−3	−2.3	–
A5	−1	10	7	5	−2.3	−2.3	1.2

TABLE 4. Same as table 3 but for the mode $n=3$.

measurements indicate a smaller velocity in the lower layer. There is therefore always a small barotropic component which tends to entrain the perturbation at a higher rotation rate.

4.4. *Comparisons with numerical simulations*

The growth of the modes $n=2$ and 3 from the numerical simulations is compared with the experiments in figure 15. In the free simulations (dashed-dot lines), the initial perturbation is smaller than in the experiments (+ signs), so the instability is delayed. However the growth rates, given by the slope in the logarithmic representation, are in good agreement.

A more precise comparison can be obtained using data assimilation. It allows one to adjust the simulation to the actual vortex structure, and to introduce the amplitude and phase of the initial perturbation. For a continuing data assimilation, the simulation provides a good fit of the experiments during the whole evolution (see solid lines). If data assimilation is performed only during the initial stage, we can compare the experiments with the appropriately initiated free model. The result, shown by the dotted line in figure 15, indicates a good agreement during the exponential growth.

The later nonlinear evolution is also very similar in the simulation and in the experiment. Nevertheless, the vortex splitting itself is a little faster in the simulation

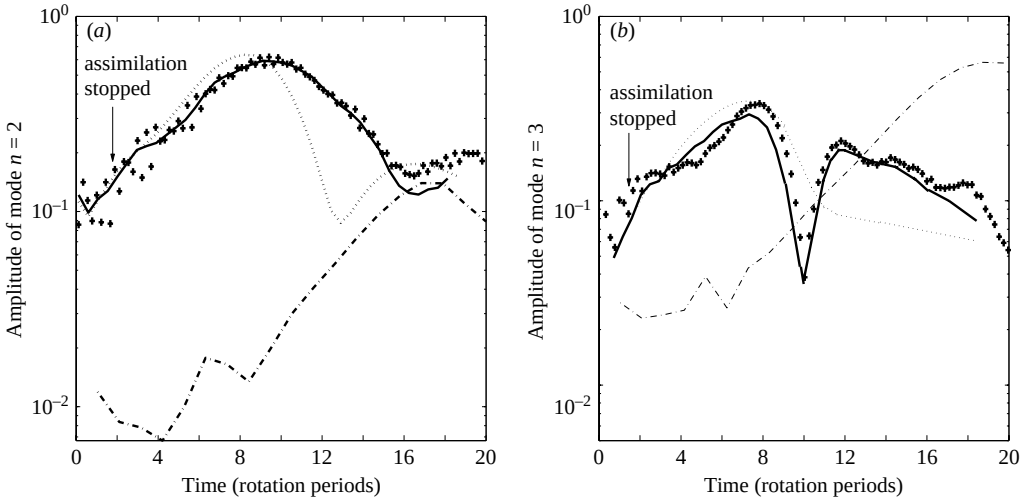

FIGURE 15. Comparison of amplitude of mode 2 (*a*) and 3 (*b*) in the upper layer for the free numerical simulation (dash-dotted line), the experiment (+), the simulation with permanent assimilation (solid line) and the free simulation initiated by five steps of data assimilation (dotted line). Experiment A3 ($\eta_0 = -12.5$ cm, $\gamma = 4.0$).

(the mode amplitude reaches a maximum at an earlier stage). This discrepancy is probably due to a limitation of the hydrostatic approximation used in the model: while the initial instability growth is fairly slow, allowing the lower layer to reach a two-dimensional state, the final splitting is faster, and involves a small horizontal scale, so that the hydrostatic approximation may not be very well satisfied.

5. Nonlinear development of the perturbation and final organization

5.1. *Formation of hetons*

After the growth of the baroclinic instability, we always observe that each crest of the instability moves outward as a translating dipole. This process is clearly visible in figure 16, showing the PV fields obtained by data assimilation in the case of a dominant mode $n = 2$. Similarly, three dipoles are observed when the mode $n = 3$ is dominant. Note that the method of data assimilation allows extrapolation of the fields beyond the zone of PIV measurements, represented by the dotted square in figure 16: the measured velocity is used to guide the flow computation performed in the larger domain. The quality of this 'guiding' is validated by the r.m.s. difference between the measurements and numerical model, which remains at the order of the measurement errors (see Galmiche *et al.* 2003).

In an ideal contour dynamics computation, the dipoles couple a PV patch in the upper layer with a PV patch of opposite sign in the lower layer. Each PV patch induces a velocity in both layers, entraining its companion in the translating motion. This structure has been called a 'heton' by Hogg & Stommel (1985).

In the present experiments, as shown for instance in figure 16 for $\eta_0 < 0$, the dipole is indeed mainly composed of a negative vortex in the upper layer and a positive one in the lower layer (or the opposite signs for $\eta_0 > 0$). It also contains, however, a positive PV patch in the upper layer. This has been formed by collecting positive

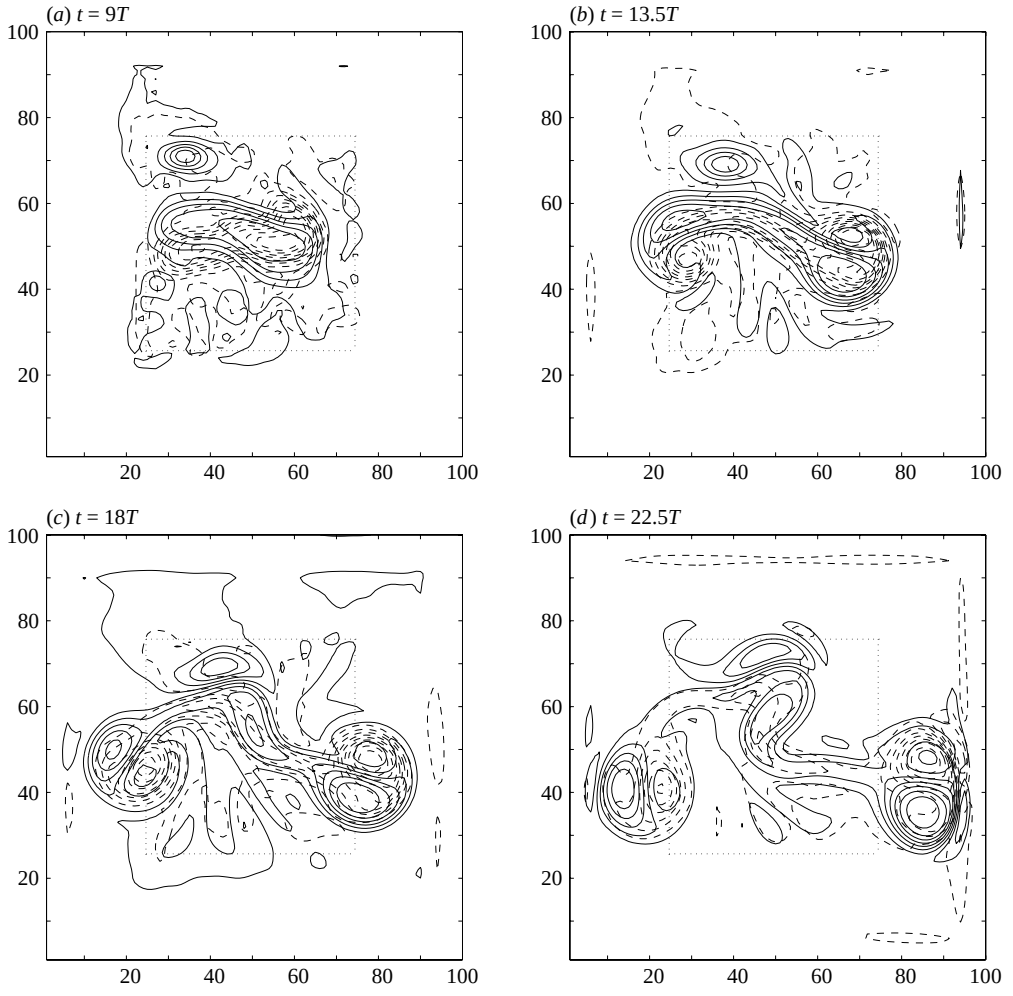

FIGURE 16. Potential vorticity anomaly in the upper layer (solid line) and in the lower layer (dashed line) at successive times, showing the organization into dipoles (hetons). The dotted square corresponds to the field of PIV measurement. Same experiment as in figure 14, and same iso-values. The axis unit is the grid mesh, equal to 5 cm (used for both computations and PIV measurements).

PV perturbations initially present in the upper layer. Therefore in the general case, vortex couples of opposite signs are formed, each containing a component in both layers. In the numerical simulations, we observe that a monopole can also remain at the position of the initial vortex, but this occurs for higher $\gamma(>5)$ which we did not study experimentally. We can conjecture that any localized excitation in such a two-layer system tends to self-organize into circular monopoles or vortex dipoles in steady motion. We observe this phenomenon as a general result. For instance, during 'bad' experiments, polluted by a strong initial perturbation, a highly perturbed initial field tends to self-organize into dipoles or monopoles.

5.2. *Cyclone–anticyclone asymmetry*

In the QG limit, the flow dynamics is independent of the sign of η_0: changing the sign just changes cyclones into anticyclones, with a mirror symmetric motion. For high amplitudes $|\eta_0/H_1|$ we expect genuine asymmetries however. Experimentally,

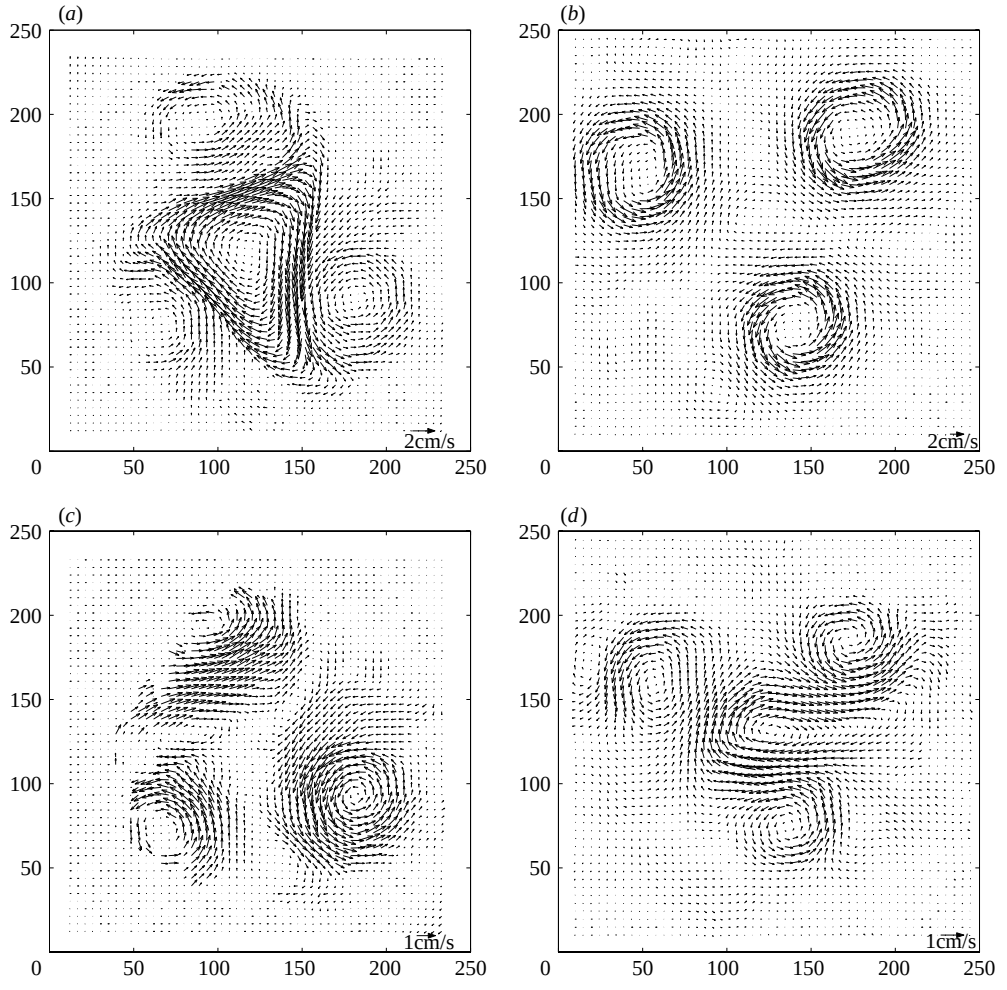

FIGURE 17. Horizontal velocity fields with well-developed perturbations for an anticyclone (a, c, experiment A5) and a cyclone (b, d, experiment C3). The upper layer is represented on the top graphs (a, b) and the lower layer on the lower graphs (c, d). The scale is in cm (domain 250 cm $\times$ 250 cm).

we observe an obvious qualitative difference, as shown in figure 17. The general observation is that cyclones, unlike anticyclones, tend to be intense and compact, and correlated in both layers, with a strong barotropic component. For instance in figure 17(a), the anticyclonic vortex in the upper layer is being stretched in the threefold instability. At the same time, the cyclone in the lower layer has been split and reorganized into three coherent vortices. Each of these vortices induce a cyclonic motion in the upper layer. A similar behaviour occurs when the cyclone is in the upper layer, as shown on figure 17(b), permuting the layers: compare figures 17(b) and 17(c), as well as figures 17 (a) and 17(d). The observed difference between cyclones and anticyclones is therefore a genuine effect, independent of the layer depths.

Using numerical simulations, we can check that the cyclonic PV indeed tends to organize into compact vortices, while the anticyclonic PV tends to be stretched. Such a compact cyclonic vortex induces a strong cyclonic velocity in both layers.

This difference can be understood by comparing the velocity fields induced by a positive or negative PV patch with the same modulus, see equation (3.3). For a positive anomaly, the cyclo-geostrophic term in v^2/r adds to the geostrophic term fv, which results in a stronger slope, and a more intense velocity field. This more intense velocity in turn favours local roll-up of PV rather than stretching, producing a compact circular vortex.

6. Conclusions

In this work, two classical processes of geophysical fluid dynamics have been quantitatively investigated in laboratory: the cyclo-geostrophic adjustment and the baroclinic instability of the resulting vortex. Owing to the large size of the rotating tank, the inertial regimes of oceanic or atmospheric dynamics can be better approached than is possible for smaller-scale experiments.

The cyclo-geostrophic adjustment occurs by damped inertial oscillations. This damping is achieved within a few rotation periods by turbulent friction and the emission of inertio-gravity waves. The velocity profile in the resulting axisymmetric vortex can be estimated by the conservation of potential vorticity. However, systematic deviations from this prediction are observed, and are attributed to the intense turbulent mixing occurring in the initial gravity currents. Such potential vorticity mixing by small-scale turbulence can be quite influential for ocean dynamics (Morel & McWilliams 2001), but it is still not well understood. Since this effect is beyond the hydrostatic approximation, the influence of the aspect ratio L_R/H_1 should be important, and this should be explored by further experiments with larger horizontal scales.

Baroclinic instability develops on a longer time scale, quite distinct from the inertial oscillations. Unlike the adjustment process, this baroclinic instability occurs in a hydrostatic regime, with velocity independent of height in both layers. This 'shallow water' regime, remarkably, occurs even for a lower layer thicker than the flow horizontal scale. It is argued that the hydrostatic approximation should apply to the baroclinic instability as long as the vertical interface displacement is not greater than the smallest internal Rossby radius of deformation, which is also the typical horizontal scale. Employing the method of data assimilation, the hydrostatic model has been shown to apply also in the nonlinear regime. Small discrepancies, however, are observed at a late state of the instability: the vortex break-up is a little faster in the model than in the experiment, but otherwise quite similar. The emission of inertio-gravity waves may play a role during this intense break-up event, but it was not detected among the ambient residual wave background.

We find that this growth of baroclinic instability is in good agreement with the quasi-geostrophic theory, even for large amplitudes $|\eta_0|/H_1$. This applies even in the extreme case of an interrupted upper layer, provided we take the reference interface position at the middle of the initial step, using the effective parameters (3.8)–(3.9). This confirms stability analysis with the two-layer shallow water system (Boss *et al.* 1996): the long-wave instability modes are described well by the quasi-geostrophic approximation even for $|\eta_0|/H_1 \sim 1$. Short-wave instabilities are also predicted by theory. These are active during the cyclo-geostrophic adjustment, contributing to small-scale turbulence, as observed by Stegner *et al.* (2004). We also observe the growth of small-scale perturbations in the visualization of figure 4(*c*). However, these rapid instabilities are quickly damped, and the system relaxes to an axisymmetric state before the growth of baroclinic instability, which dominates the flow evolution

on a longer time scale: the fastest growing modes are therefore not the most relevant here, contrary to common opinion.

In summary, the growth rate predicted by the quasi-geostrophic theory, with a basic flow made of a disk of uniform potential vorticity, always agrees with experiments within a factor of two. This is reasonable taking into account the idealization of the basic flow and the experimental uncertainty. The results agree well with the prediction from the Phillips model, for a horizontally uniform effective velocity equal to half the extremum vortex velocity. The relevance of the classical Phillips model for the instability of baroclinic vortices has been checked previously by Griffiths & Linden (1981*a*). Here a more precise analysis of the growth rates is provided. Furthermore it is shown experimentally that the upper-layer velocity perturbations lag the lower-layer ones by a constant phase difference of 1 rad. This appears to be a very robust feature, persisting far into the nonlinear regime, which fundamentally characterizes the layer coupling during baroclinic instability.

The development of the baroclinic instability ends in the vortex splitting and reorganization into translating dipoles. This reorganization was observed previously in the experiments of Griffiths & Linden (1981*a*) and in various numerical simulations. We confirm that this reorganization into vortex dipoles, with variable components in the upper and lower layers, is quite general and persists at high Reynolds number. This is reminiscent of what is observed for the two-dimensional incompressible Euler system, and it can be explained by general arguments of statistical mechanics for vorticity (Chavanis & Sommeria 1998). Generalization of this theory to the shallow-water system by Chavanis & Sommeria (2002) could explain the same phenomenon for the two-layer system.

It is found that for large amplitudes η_0/H_1 this reorganization involves a clear asymmetry between anticyclones and cyclones: the latter are more compact and barotropic than anticyclones. A cyclone splits into coherent cyclones (like in figure 17*b*), while an anticyclone develops coherent cyclones on its periphery, with a deep barotropic 'root' in the lower layer. This difference can be understood by simple arguments about potential vorticity inversion for an axisymmetric state. These results are in agreement with oceanic observations of vortex instability for cyclones (Kennelly *et al.* 1985) and anticyclones (Richardson *et al.* 1979).

Note that a predominance of large anticyclones is commonly observed in shallow-water experiments, which seems in contradiction with our results. The two-layer system is in fact quite different from the reduced-gravity shallow-water system obtained in the limit of a deep lower layer. Let us imagine that a large vortex has been produced in the upper layer, for instance through a merging process. This vortex is unstable unless the lower layer thickness H_2 is such that $H_2/H_1 > \gamma^4/4$, which strongly increases with the normalized vortex size $R/L_R = \gamma$: for instance to stabilize vortices with $\gamma = 3$, we would need $H_2/H_1 > 20$. The two-layer system therefore converges only slowly to the shallow-water reduced-gravity system.

Finally the method of data assimilation employed provides interesting perspectives in itself. It allows one to extrapolate experimental results, providing for instance the interface displacement and potential vorticity fields. It provides a validity test of the dynamical model at various stages of the evolution: the baroclinic instability process can be initiated with the experimentally measured velocity profile and perturbation. It also allows fundamental questions of predictability and controllability of the system, in a real turbulent fluid system, to be addressed as discussed in Galmiche *et al.* (2003): the growth of the baroclinic instability can be viewed as a very simplified realization of mid-latitude weather perturbations. Nevertheless, we did not try more simple

methods, using balance assumptions, for the initialization of the computations, so we do not claim that the method of data assimilation which we employed is superior for that purpose.

We would like to acknowledge H. Didelle, S. Mercier and S. Viboud for technical support for the experiments, as well as Y. Morel, P. Brasseur and J. Verron for help in implementing the numerical model with the data assimilation code SESAM. We thank A. Stegner and X. Carton for their comments on our results. This work has been supported by the Service Hydrographique et Océanographique de la Marine under grant number 00.87.071.00.470.29.25.

REFERENCES

Baey, J.-M. & Carton, X. 2002 Vortex multipoles in two-layer rotating shallow-water flows. *J. Fluid Mech.* **460**, 151–175.

Bleck, D. & Boudra, D. 1986 Wind driven spin-up in eddy-resolving ocean models formulated in isopycnic coordinates. *J. Geophys. Res.* **91**, 7611–7621.

Boss, E., Paldor, N. & Thompson, L. 1996 Stability of a potential vorticity front: from quasi-geostrophy to shallow water. *J. Fluid Mech.* **315**, 65–84.

Bouruet-Aubertot, P. & Linden, P. F. 2002 The influence of the coast on the dynamics of upwelling fronts. *Dyn. Atmos. Oceans* **36**, 153–173.

Bretherton, F. 1966 Baroclinic instability and the short wavelength cut-off in terms of potential vorticity. *Q. J. Met. Soc.* **92**, 335–345.

Carton, X. 2001 Hydrodynamical nodeling of oceanic vortices. *Surveys Geophys.* **22**, 179–263.

Charney, J. G. & Stern, M. E. 1962 On the instability of internal baroclinic jets in a rotating atmosphere. *J. Atmos. Sci.* **19**, 159–172.

Chavanis, P. H. & Sommeria, J. 1998 Classification of robust isolated vortices in two-dimensional hydrodynamics. *J. Fluid Mech.* **356**, 259–296.

Chavanis, P. H. & Sommeria, J. 2002 Statistical Mechanics of the shallow water system. *Phys. Rev* E **65**, 026302.

Chia, F., Griffiths, R. W. & Linden, P. F. 1982 Laboratory experiments on fronts. Part 2 the formation of cyclonic eddies at upwelling fronts. *Geophys. Astrophys. Fluid Dyn.* **19**, 189–206.

Fincham, A. & Delerce, G. 2000 Advanced optimization of correlation imaging velocimetry algorithms. *Exps. Fluids* [Suppl.] S13–S22.

Fincham, A. M. & Spedding, G. R. 1997 Low cost, high resolution DPIV for measurement of turbulent fluid flow. *Exps. Fluids* **23**, 449–462.

Galmiche, M., Sommeria, J., Thivolle-Cazat, E. & Verron, J. 2003 Using data assimilation in numerical simulations of experimental geophysical flows. *C. R. Acad. Sci.* **331/12**, 843–848.

Griffiths, R. W. & Linden, P. F. 1981*a* The stability of vortices in a rotating, stratified fluid. *J. Fluid Mech.* **105**, 283–316.

Griffiths, R. W. & Linden, P. F. 1981*b* The stability of buoyancy-driven coastal currents. *Dyn. Atmos. Oceans* **5**, 281–306.

Hide, R. & Masson, P. J. 1975 Sloping convection in a rotating fluid. *Adv. Phys.* **24**, 47–100.

Hogg, N. & Stommel, H. 1985 The heton, an elementary interaction between discrete baroclinic geostrophic vortices, and its implications concerning eddy het flow. *Proc. R. Soc. Lon.* A **397**, 1–20.

Holford, J. M. & Dalziel, S. B. 1996 Measurements of layer depth during baroclinic instability in a two-layer flow. *Appl. Sci. Res.* **56**, 191–207.

Hoskins, B. J., Mc Intyre, M. E. & Robertson, A. W. 1985 On the use and significance of isentropic potential vorticity maps. *Q.J.R. Met. Soc.* **111**, 877–946.

Kennelly, M. A., Evans, R. H. & Joyce, T. M. 1985 Small-scale cylones on the periphery of a Gulf Stream warm-core ring. *J. Geophys. Res.* **90**, 8845–8857.

Kuo, A. C. & Polvani, L. M. 2000 Nonlinear geostrophic adjustment, cyclone/anticyclone asymmetry, and potential vorticity rearrangement. *Phys. Fluids* **12**, 1087–1100.

Morel, Y. & McWilliams, J. 2001 Effects of isopycnal and diapycnal mixing on the stability of oceanic currents. *J. Phys. Oceanogr.* **31**, 2280–2296.

Pedlosky, J. 1979 *Geophysical Fluid Dynamics.* Springer.

Pham, D., Verron, J. & Roubaud, M. 1998 A Singular Evolutive Extended Kalman filter for data assimilation in oceanography. *J. Mar. Sci.* **16**, 323–340.

Phillips, N. A. 1954 Energy transformations and meridional circulations associated with simple baroclinic waves in a two level quasi-geostrophic model. *Tellus* **6**, 273–286.

Pierrehumbert, R. T. & Swanson, K. L. 1995 Baroclinic Instability. *Annu. Rec. Fluid Mech.* **27**, 419–467.

Read, P. L., Bell, M. J., Johnson, D. W. & Small, R. M. 1992 Quasi-periodic and chaotic flow regimes in a thermally driven rotating fluid annulus *J. Fluid Mech.* **238**, 599–632.

Richardson, P. L., Maillard, C. & Stanford, T. B. 1979 Physical structure and life history of cyclone Gulf-Stream ring Allen. *J. Geophys. Res.* **84**, 7727–7741.

Rossby, C. G. 1938 On the mutual adjustment of pressure and velocity distribution in certain current systems. *J. Mar. Res.* **1**, 238–263.

Saunders, P. M. 1973 The instability of a baroclinic vortex. *J. Phys. Oceanogr.* **3**, 61–65.

Sokolovskiy, M. A. & Verron, J. 2000 Finite-core instability and interactions. *J. Fluid Mech.* **423**, 127–154.

Stegner, A., Bouruet-Aubertot, P. & Pichon, T. 2004 Nonlinear adjustment of density fronts. Part 1. The Rossby scenario and the experimental reality. *J. Fluid Mech.* **502**, 335–360.

Stegner, A. & Dritschel, D. G. 2000 A numerical investigation of the stability of isolated shallow water vortices. *J. Phys. Oceanogr.* **30**, 2562–2573.

Verron, J. & Valcke, S. 1994 Scale-dependent merging of baroclinic vortices. *J. Fluid Mech.* **264**, 81–106.

Verzicco, R., Lalli, F. & Campana, E. 1997 Dynamics of baroclinic vortices in a rotating, stratified fluid: a numerical study. *Phys. Fluids* **9**, 419–432.